



Laser-dilatometer calibration using a single-crystal silicon sample

Ines Hamann, Josep Sanjuan, Ruven Spannagel, Martin Gohlke, Gudrun Wanner, Sönke Schuster, Felipe Guzman & Claus Braxmaier

To cite this article: Ines Hamann, Josep Sanjuan, Ruven Spannagel, Martin Gohlke, Gudrun Wanner, Sönke Schuster, Felipe Guzman & Claus Braxmaier (2019) Laser-dilatometer calibration using a single-crystal silicon sample, International Journal of Optomechatronics, 13:1, 18-29, DOI: [10.1080/15599612.2019.1587117](https://doi.org/10.1080/15599612.2019.1587117)

To link to this article: <https://doi.org/10.1080/15599612.2019.1587117>



© 2019 The Author(s). Published with license by Taylor & Francis Group, LLC



Published online: 16 Apr 2019.



Submit your article to this journal [↗](#)



Article views: 915



View related articles [↗](#)



View Crossmark data [↗](#)



Citing articles: 1 View citing articles [↗](#)

Laser-dilatometer calibration using a single-crystal silicon sample

Ines Hamann^{a,b}, Josep Sanjuan^b, Ruven Spannagel^b, Martin Gohlke^b, Gudrun Wanner^c, Sönke Schuster^c, Felipe Guzman^b, and Claus Braxmaier^{a,b}

^aCenter of Applied Space Technology and Microgravity (ZARM), University of Bremen, Bremen, Germany;

^bDeutsches Zentrum für Luft- und Raumfahrt, Institute of Space Systems (DLR-RY), Bremen, Germany; ^cMax Planck Institute for Gravitational Physics (Albert Einstein Institute) and Institute for Gravitational Physics of the Leibniz Universität Hannover, Hannover, Germany

ABSTRACT



Marginal changes in geometrical dimensions due to temperature changes affect the performance of optical instruments. Highly dimensionally stable materials can minimize these effects since they offer low coefficients of thermal expansion (CTE). Our dilatometer, based on heterodyne interferometry, is able to determine the CTE in 10^{-8} K^{-1} range. Here, we present the improved interferometer performance using angular measurements via differential wavefront sensing to correct for tilt-to-length coupling. The setup was tested by measuring the CTE of a single-crystal silicon at 285 K. Results are in good agreement with the reported values and show a bias of less than 1%.

KEYWORDS

Dilatometry; silicon; differential wavefront sensing; simulation

1. Introduction

Dimensional stability of structures in high-precision and high-sensitivity optical instruments is crucial in current and future space missions. For instance, LISA Pathfinder^[1–3], launched in December 2015, measured the distance between two free-floating test masses by means of a Mach–Zehnder interferometer with sub-picometer precision in the milli-Hertz range in order to test key technologies for the Laser Interferometer Space Antenna (LISA). The Gravity Recovery and Climate Experiment Follow-on (GRACE-FO), launched in May 2018^[4], includes a laser ranging interferometer^[5,6] (LRI) to measure the distance between two spacecraft 200 km apart at the nanometer level in order to monitor changes in the gravity field of the Earth. For this purpose, it relies on a large corner cube, the so-called triple mirror assembly (TMA), which is made of a carbon fiber reinforced polymer (CFRP) structure to support the Zerodur mirrors. This material combination was proved to offer the needed dimensional stability at the nanometer level at room temperature.^[7] The Global Astrometric Interferometer for Astrophysics^[8] (GAIA) mission is another example where dimensional stability is critical: its mirrors and support are made of silicon carbide structures and need stabilities at the picometer and picoradian level in a cold environment^[9,10] ($\approx 100 \text{ K}$). The future spaceborne gravitational wave detector, LISA, will also require extremely stable optical assemblies such as optical benches and telescopes. Their stabilities are in the picometer and picoradian level over a time scale of thousands of seconds.^[11,12]

CONTACT Ines Hamann  ines.hamann@dlr.de  Deutsches Zentrum für Luft- und Raumfahrt, Institute of Space Systems (DLR-RY), 28359 Bremen, Germany.

Color versions of one or more of the figures in the article can be found online at www.tandfonline.com/uopt.

© 2019 The Author(s). Published with license by Taylor & Francis Group, LLC

This is an Open Access article distributed under the terms of the Creative Commons Attribution License (<http://creativecommons.org/licenses/by/4.0/>), which permits unrestricted use, distribution, and reproduction in any medium, provided the original work is properly cited.

Nomenclature

a	signal amplitude	L	sample's nominal length
ADC	analog-to-digital converter	M1	upper mirror
AOM	acousto-optic modulator	M2	lower mirror
ASD	(S) amplitude spectral density	\wedge	laser's wavelength
BS	beamsplitter	$\lambda/2$	half-wave plate
CTE	(α) coefficient of thermal expansion	$\lambda/4$	quarter-wave plate
d	beam spacing	N	number of data points
DWS	(η) differential wavefront sensing	PBS	polarizing beamsplitter
Δf	frequency change	ϕ	optical phase
ΔL	length change	Pt100	platinum resistor based temperature sensor
ΔT	temperature change	QPD	quadrant photo detectors
FFT	(\mathcal{F}) fast Fourier transform	SCS	single-crystal silicon
FPGA	field programmable gate array	T	temperature
f	frequency	θ	angle of the sample
i	complex unit	TTL	(β) tilt-to-length
IfoCAD	software library for the design and simulation of laser interferometers	u	uncertainty
j	index variable	X	dummy signal
k	DWS scaling factor		

Dimensional stability depends ultimately on the material's coefficient of thermal expansion (CTE) and the temperature fluctuations at which it is exposed. Thus, accurate CTE determination is crucial in the design of the instruments aboard the aforementioned missions and any space mission with similar requirements: given the thermal environment of the spacecraft, one can select the proper material or, vice-versa, given the material of the instrument, the thermal environment stability requirement can be set. CTE measurements are especially important for materials such as CFRP since their CTEs depend on the manufacturing process. Precise CTE knowledge is also key when designing composite materials to achieve virtual zero CTE at a given temperature. To validate these designs and manufacturing processes, the materials have to be characterized, which can be done with a dilatometer to obtain the CTE. We operate a laser-interferometric dilatometer, which allows CTE characterization in a temperature range from 140 K to 250 K with uncertainty levels of 10^{-8} K^{-1} ^[13]. Unique to this dilatometer is its interferometric read-out, which gives information about length change and sample tilting. With this nearly force-free optical measurement, the sample remains unconstrained during thermalization.

In this manuscript, we present the latest results of our dilatometer, which allows us to characterize CTEs at the 10^{-8} K^{-1} level. Our previous setup^[13] was found to be limited by tilt-to-length coupling, i.e. a tilt of the sample under test introduced an error in the length measurement that could not be corrected since the setup was unable to measure angles. Consequently, a systematic bias of a few percent was present in the CTE determination. In this paper, the tilt-to-length errors are investigated via simulations and experiments. As a result, the most dominant systematic effect has been identified as the sample's tilt, which can be corrected by measuring it and subtracting it in post-processing. In order to do so, the laser-interferometric dilatometer has been improved by including quadrant photo detectors (QPDs) and differential wavefront sensing (DWS)^[14] measurement capabilities. The correction method has been validated by measuring the CTE of a single-crystal silicon (SCS) sample, which serves as a reference with a well-defined CTE reported in the literature. The bias in the CTE estimation has been reduced from approximately 7% to less than 1%.

The manuscript is organized as follows: [Section 2](#) describes the setup, the optical simulation model and the setup improvements to cope with tilt-to-length (TTL) coupling. [Section 3](#) focuses on the dilatometer characterization in terms of noise levels and TTL coupling coefficients. [Section 4](#)

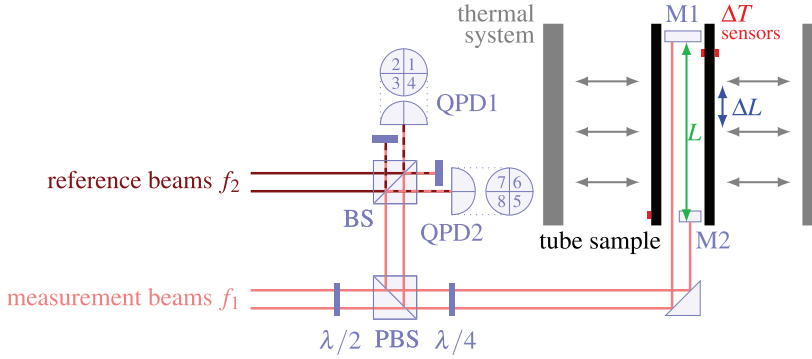


Figure 1. Simplified interferometric setup. f_1 represents the measurement beams, which pass the half-wave plate ($\lambda/2$), the polarizing beamsplitter (PBS), the quarter-wave plate ($\lambda/4$), and are reflected off the mirrors M1 and M2. After reflection, the beams pass again the $\lambda/4$ and are now reflected by the PBS toward the beamsplitter (BS) where they are superimposed to the reference beams f_2 . Quadrant photo detector QPD1 and QPD2 measure phase changes generated by a path length variation ΔL . The temperature variation ΔT of the sample is caused by the thermal system and measured by Pt100 sensors. The distance between the mirrors M1 and M2 defines the nominal length L .

describes the actual CTE measurement of the SCS, the correction applied to eliminate TTL errors and details the sources of uncertainty. A conclusion and outlook are given in [Section 5](#).

2. Setup description

A short description of the setup with the latest upgrades is given in the following. A detailed description of our setup is given in our previous publication^[13]. Our dilatometer is split into several subsystems. First, the laser module uses an iodine-based frequency stabilization at 532 nm^[15] and at the same time provides a laser beam at 1064 nm, which is sent to the second subsystem: the heterodyne frequency generation, where two beams are frequency shifted by two acousto-optic modulators (AOMs) to have a frequency difference of 10 kHz. These two beams are guided to the vacuum chamber by optical fibers and led to the third subsystem, the heterodyne interferometer for optical measurements with electronic read-out. The fourth subsystem is the thermal one that controls the sample's temperature.

[Figure 1](#) shows a simplified schematic of the interferometer and thermal systems inside the vacuum chamber. A tube-shaped sample, with clamped mirrors at the end faces, is placed inside the thermal system. This setup allows us to measure the linear coefficient of thermal expansion, CTE, which is defined as

$$\alpha(T) = \frac{1}{L(T)} \cdot \frac{\Delta L(T)}{\Delta T(T)}. \quad (1)$$

The nominal length L is given by the distance between the mirrors M1 and M2. The thermal system is able to cool down or heat up the sample. Pt100 sensors on the sample's surface measure the temperature change ΔT . As indicated in [Figure 1](#), two sensors are placed on the sample tube's outer surface nearby the sample mirrors, whereas the third sensor is placed on the inner surface. The generated path length variation ΔL is calculated from the phase difference between the beams reflecting off M1 and M2, which are obtained by interfering them with reference beams that generate beat-notes at 10 kHz. Their phases are measured by the phasemeter.

Since our interferometer is equipped with quadrant photo detectors (QPDs), phase changes on these detectors can be used for differential wavefront sensing (DWS)^[14]. DWS measures the tilt between the wavefronts of the interfering beams in the QPDs and, consequently, any tilt from M1, M2, or the whole sample will generate a DWS signal.

The four quadrant signals of each QPD can be evaluated in different ways to derive a tilt information of the wavefronts. A common approach^[16] is to compare QPD halves (two-by-two quadrants) to determine horizontal tilt from yaw-induced motions and vertical tilt from pitch-induced motions. Because of the horizontal spacing between the measurement beams, the so-called horizontal DWS signals have a higher impact in our setup while the vertical tilt can be neglected. The horizontal DWS signals are calculated as

$$\text{QPD1: } \beta_{\text{QPD1}} = \eta_{\text{QPD1}} \cdot k_{\text{QPD1}} = ((\phi_2 + \phi_3)/2 - (\phi_1 + \phi_4)/2) \cdot k_{\text{QPD1}} \quad (2a)$$

$$\text{QPD2: } \beta_{\text{QPD2}} = \eta_{\text{QPD2}} \cdot k_{\text{QPD2}} = ((\phi_5 + \phi_8)/2 - (\phi_6 + \phi_7)/2) \cdot k_{\text{QPD2}} \quad (2b)$$

with ϕ_j as phase values of quadrant j of the photo detector (Figure 1).

The scaling factor k_{QPD} is used to convert the DWS signal from the setup's electrical phase signal to optical radians or in our case nanometers according to a mirror's tilt, i.e., it represents the tilt-to-length (TTL) coupling coefficient of our setup. Note that k_{QPD} includes two calibration factors: the one converting wavefront tilt to phase difference in the four quadrants and the actual TTL coupling, i.e., how tilting of the sample and mirrors introduce an error in length variation determination. This scaling factor is obtained by a dedicated calibration described in Section 3. Because of the reflection in the beamsplitter (BS), QPD2 receives a mirror image; therefore, the signals of quadrant 5 and 8 should be exchanged with 6 and 7, respectively. The interferometric longitudinal signal, which comprises ΔL is calculated from the phases ϕ_j and scaled by the wavelength λ :

$$\Delta L = \frac{\lambda}{4\pi} (\phi_{\text{QPD1}} - \phi_{\text{QPD2}}) = \frac{\lambda}{4\pi} \left(\frac{1}{4} \sum_{j=1}^4 \phi_j - \frac{1}{4} \sum_{j=5}^8 \phi_j \right). \quad (3)$$

In the ideal case, ΔL is derived from a longitudinal displacement of the sample mirrors as part of the sample dilatation during, for instance, a sinusoidal thermal cycling. In reality, both sample and mirror tilts will cause a measurement error in ΔL . To analyze this behavior in more detail, simulations based on IfoCAD^[16,17] were implemented. The simulated cases are shown in Figure 2 using a constant k_{QPD} , which is a simplification for easier comparison. Case (A) shows the ideal case where tilt is not considered, thus $\beta_{\text{QPD}} = 0$. Case (B) shows a potential scenario where the sample bends due to asymmetrical thermal distribution or any other source of disturbance. However, the bending does not introduce errors in the CTE estimation because the TTL effects cancel out (β_{QPD1} and β_{QPD2} have opposite signs). Case (C) shows the scenario where the mirrors' tilts are independent, i.e., each mirror tilts with respect to its own pivot point and, clearly, their tilt can introduce an error in the CTE estimation. The longitudinal measurement shows an enlarged amplitude and opposite sign, which is driven by a strong TTL coupling. Finally, case (D) shows the case where the sample and the mirrors tilt as a whole. In this scenario, the effect of the tilt on the longitudinal measurement does not cancel out: both TTL signals have the same sign. For instance, in this simulation ΔL increases from the ideal 260 nm to 279 nm, where the 19 nm difference is due to the tilt of the sample, which is measured by both β_{QPD} . Previous experiments^[13] have shown that the most likely scenario in our setup is the one described in (D), which would allow us to correct it by taking into account the DWS read-out. Consequently, in the following, we assume scenario (D), i.e., common tilt of sample and mirrors (M1 and M2).

It is clear that TTL has an impact on the length measurement, which can be mitigated by measuring it and subtracting it in post-processing. In our previous setup^[13] such functionality was not yet enabled due to problems with the optical read-out and only an estimation of the coupling was possible, which supported the behavior shown in Figure 2(D). The optical read-out has been upgraded to allow DWS measurements. It consists of three parts: a detector (quadrant photo diode and associated electronics), an analog-to-digital converter (ADC) stage and a field programmable gate array (FPGA) unit where the digital phasemeter is implemented. Our phasemeter was modified to implement more robust versions of Equations (2) and (3). This was done by

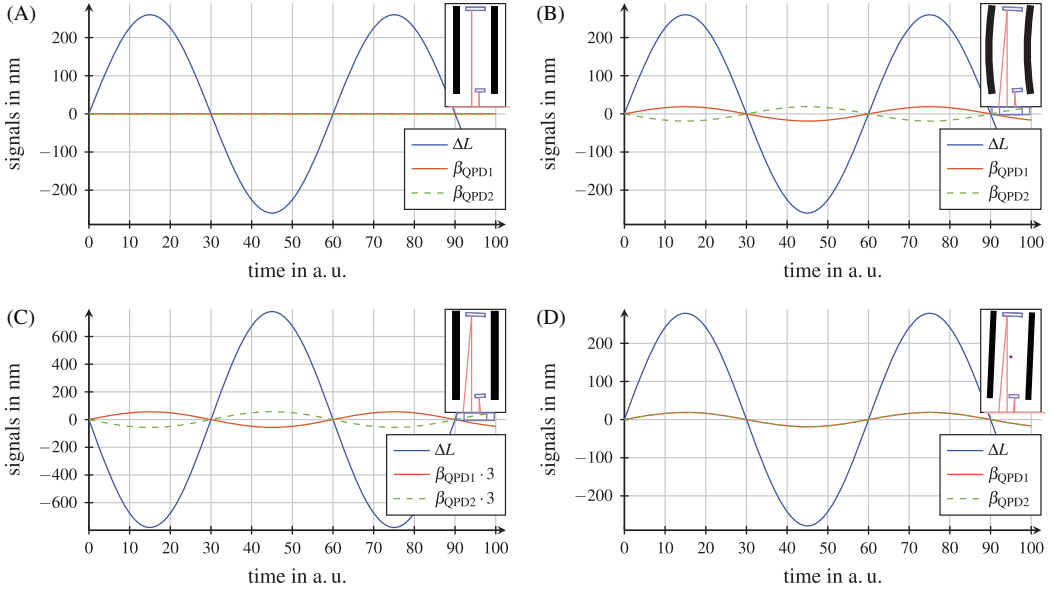


Figure 2. Simulation results of sample with clamped mirrors. The ideal case is shown in (A), where only a linear dilatation takes place. In case (B), the sample is bent, e.g. by a non-uniformly heating or other sources of mechanical stress and the tilt signals show opposite signs. Case (C) shows also inverted tilt signals, which can occur because both mirrors are clamped inside the sample and tilt independently of the sample's movement. The simulated ΔL signal is enlarged compared to (A) and shows a 180° phase offset. In case (D), both tilt signals are equal and have the same sign as the slightly increased ΔL . The increase is exactly the value of either β_{QPD1} or β_{QPD2} . This special behavior is caused by tilting of the sample around one pivot point (purple point). It enables a correction of the tilt-to-length (TTL) when the tilt can be measured with high accuracy.

including the amplitudes a_j , which weight the phase signal ϕ_j in case of non-centered beams on the QPD's surface and in addition provide more robustness in case of a phase jump.^[16,18]

$$\text{QPD1: } \beta_{\text{QPD1}} = \eta_{\text{QPD1}} \cdot k_{\text{QPD1}} = \arg\left(\frac{a_2 e^{i\phi_2} + a_3 e^{i\phi_3}}{a_1 e^{i\phi_1} + a_4 e^{i\phi_4}}\right) \cdot k_{\text{QPD1}} \quad (4a)$$

$$\text{QPD2: } \beta_{\text{QPD2}} = \eta_{\text{QPD2}} \cdot k_{\text{QPD2}} = \arg\left(\frac{a_5 e^{i\phi_5} + a_8 e^{i\phi_8}}{a_6 e^{i\phi_6} + a_7 e^{i\phi_7}}\right) \cdot k_{\text{QPD2}} \quad (4b)$$

and

$$\Delta L = \frac{\lambda}{4\pi} \left(\arg\left(\sum_{j=1}^4 a_j e^{i\phi_j}\right) - \arg\left(\sum_{j=5}^8 a_j e^{i\phi_j}\right) \right). \quad (5)$$

Finally, it is worth mentioning that our experiments typically use sine waves as driving signals. The signal's amplitude is estimated by computing its fast Fourier transform (FFT), indicated by \mathcal{F} and taking the value at the (thermal) modulation frequency f_{mod} . To avoid windowing effects, which falsify the amplitude estimation, the number of measured samples N must be an integer multiple of the sampling frequency f_{samp} divided by f_{mod} . The FFT results in a complex number, which can be converted to amplitude and phase. The corresponding uncertainty in the amplitude is derived from the noise or amplitude spectral density (ASD) $S_X(f)$ of the signal X scaled by the effective noise bandwidth of the FFT.^[2,19] For a rectangular window, the effective noise bandwidth is f_{samp}/N . The amplitude and its uncertainty are calculated as

$$X|_{f=f_{\text{mod}}} = 2 \cdot |\mathcal{F}(X)|/N \pm S_X(f_{\text{mod}}) \cdot \sqrt{f_{\text{samp}}/N}, \quad (6)$$

where the uncertainty is given for $1-\sigma$ (67% confidence interval).

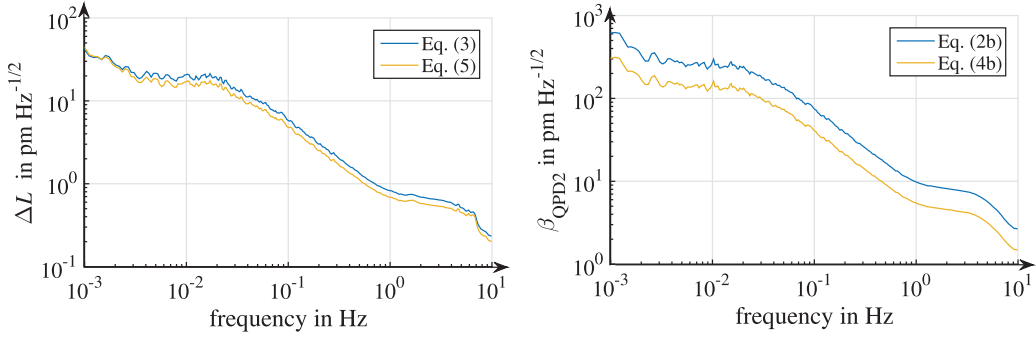


Figure 3. ASDs for ΔL (left) and β_{QPD2} (right) improved optical signal read-out in interferometer.

3. Interferometer characterization

The noise of the interferometer in the dilatometer setup was characterized as described in the following. The measurement beams were reflected off a fixed single mirror instead of the two separated mirrors M1 and M2. The results, computed by LTPDA toolbox,^[20] are shown in **Figure 3** as ASDs for ΔL and for β_{QPD2} (β_{QPD1} exhibited similar results). The blue traces show the noise levels when using **Equations (2b) and (3)**. They are 40 pm Hz^{-1/2} for ΔL and 600 pm Hz^{-1/2} for β_{QPD2} at 1 mHz and rolling off towards higher frequencies. The yellow traces show the results when using **Equations (4b) and (5)**. A factor of two improvements is observed in the β_{QPD2} measurement over the whole frequency range.

The DWS scaling factors, k_{QPD} , which are needed to correct errors introduced by TTL coupling, are derived from a calibration procedure where the measurement beams are reflected off a motorized tip-tilt mirror [Newport FSM 300] placed instead of M1 (**Figure 1**). The TTL coupling is assumed to be independent of the position of the motorized tip-tilt mirror. As stated in **Section 2**, previous experiments support the tilting scenario described in **Figure 2(D)**, i.e., the sample and the mirrors tilt together around the support mount of the sample. In this case, the TTL error can be approximated by^[13]

$$\Delta L_{\text{TTL}} \simeq d \cdot \theta, \quad (7)$$

where d is the separation between the measurement beams, θ is the horizontal angle of the sample and ΔL_{TTL} is the associated length error due to θ . Our calibration procedure has the same expression for the TTL coupling since the pivot point of the motorized mirror is located at the center of the mirror. Consequently, the coupling coefficients obtained with the calibration measurement should be applicable to the CTE measurements where the whole sample tilts.

The noise levels of the calibration measurement are shown in **Figure 4** and are needed in order to calculate uncertainties in the k_{QPD} coefficient according to **Equation (8)**, which is, in turn, needed to calculate η_{QPD} .

The actual calibration measurement consisted of tilting the motorized mirror at a frequency of 0.5 Hz and a total time of 320 s (= 6400 samples at 20 Hz sampling frequency). The amplitude was adjusted to approx. 5 μrad , 14 μrad , 30 μrad , 50 μrad , 90 μrad and 160 μrad every 55 s to calibrate this angular range. The interferometric signals are plotted in **Figure 5** in the time and the frequency domains. The DWS scaling factors are calculated from the amplitudes at the modulation frequency as

$$k_{\text{QPD}} = \frac{\Delta L}{\eta_{\text{QPD}}} \pm \sqrt{\left| \frac{u\Delta L}{\eta_{\text{QPD}}} \right|^2 + \left| \frac{\Delta L \cdot u\eta_{\text{QPD}}}{(\eta_{\text{QPD}})^2} \right|^2} \quad (8a)$$

$$k_{\text{QPD1}} = 787.4 \text{ nm/rad}_{\text{elec}} \pm 0.1 \text{ nm/rad}_{\text{elec}} \quad (8b)$$

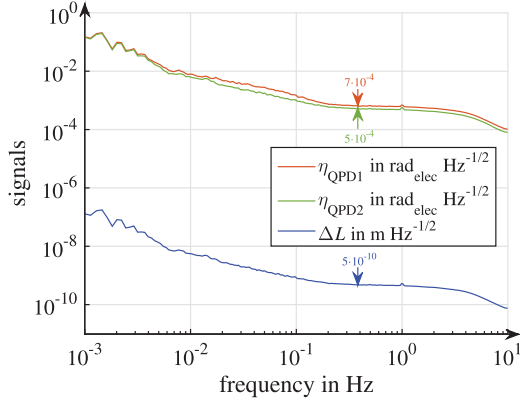


Figure 4. ASDs of optical setup with tip-tilt mirror.

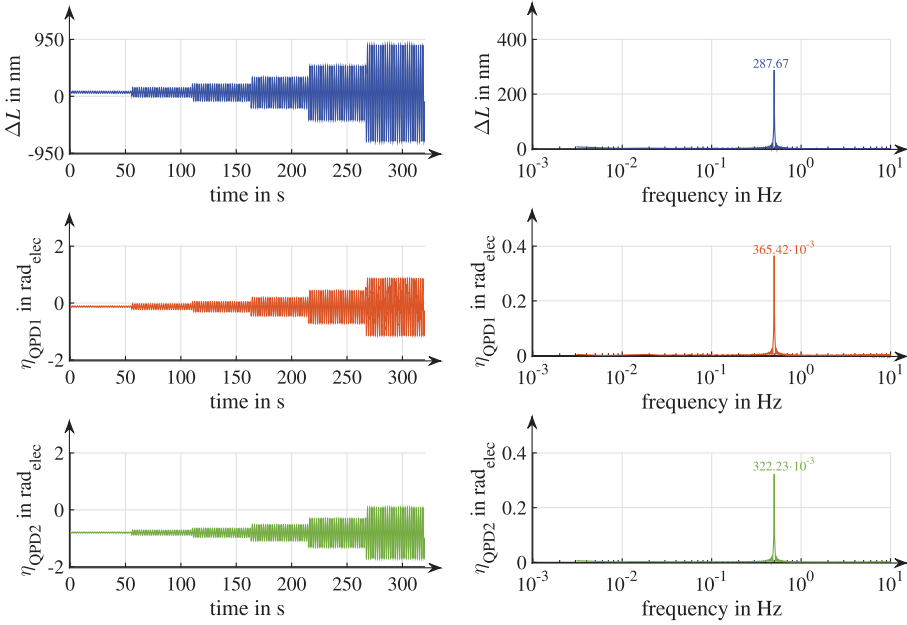


Figure 5. Tilt calibration measurement results for ΔL (top), η_{QPD1} (middle), and η_{QPD2} (bottom) in time- (left) and frequency-domain (right).

$$k_{\text{QPD2}} = 892.9 \text{ nm/rad}_{\text{elec}} \pm 0.1 \text{ nm/rad}_{\text{elec}}, \quad (8c)$$

where $u\Delta L = 30 \text{ pm}$, $u\eta_{\text{QPD1}} = 40 \mu\text{rad}_{\text{elec}}$ and $u\eta_{\text{QPD2}} = 30 \mu\text{rad}_{\text{elec}}$ and both terms under the square root drive the uncertainty equally. This uncertainty does not include the unknown uncertainty caused by the tip-tilt mirror itself in terms of longitudinal movements during rotation and effects due to the beam position on the mirror to its rotational center.

The difference between the scaling factors is driven by the signal's offset, which is larger for η_{QPD2} than for η_{QPD1} . The individual offset on each QPD is caused by the (initial) misalignment between the measurement and reference beams wavefronts. This (initial) misalignment is driven by a deviation of parallelism from within the two reference beams or the two measurement beams and also from both beam pairs to each other. Therefore k_{QPD} depends on the misalignment offset. In agreement with simulations, an increase of the initial tilt also increases the scaling factor k_{QPD} .

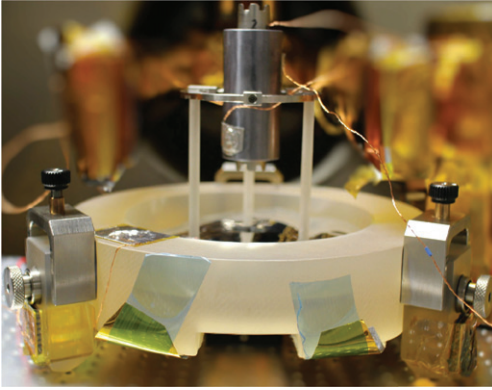
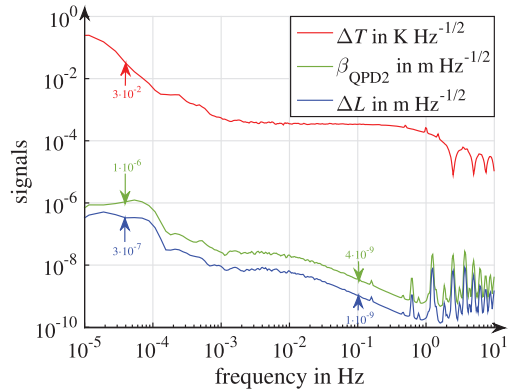


Figure 6. Photograph of SCS in sample support (left) and ASDs used for uncertainty estimation (right).



4. Sample measurement

To verify the accuracy and systematic uncertainties of our dilatometer with respect to the CTE measurements we have chosen single-crystal silicon (SCS) as a sample material. Silicon is a standard reference material for expansion measurements. It is available in extremely high-purity form and can be used over a wide temperature range for calibration purposes based on its high melting temperature. The CTE has been well studied^[21–24] for many years. Our sample was processed by Freiburger Silicium GmbH from a $\langle 100 \rangle$ float-zone silicon in a tube shape size with outer diameter of 28 mm to fit in our sample support and inner diameter of 20 mm to provide grip for our mirror mounts.

The sample with equipped mirror mounts placed in the sample support is shown in **Figure 6** (left) together with the setup's ASD results for uncertainty estimation (right) based on **Equation (6)**. The noise levels were measured during a quiet run, i.e., without applying any thermal excitation. A description of the mechanical setup is given in our previous publication^[13]. We performed the CTE determination at 285 K, which is split into two measurements. First, a measurement at constant temperature to derive L accurately and, second, a measurement with cycled temperature to estimate ΔT , ΔL , and η_{QPD} . From both results, the CTE value, α , is calculated.

4.1. Measurement at constant temperature

Using a vacuum chamber enables a homogeneous radiative heat exchange between the thermal system and the sample. A constant cooling rate is generated by a helium pulse tube cooler, which is compensated by resistive heaters to apply thermal profiles to the sample. We use three Pt100 sensors [IST P0K1.161.6W.Y.010] on the sample's surface to measure the temperature variation and distribution across the sample (**Figure 1**). The natural deviation of the sample's Pt100 sensors was corrected by cross-calibrating the values from a long term measurement, while the temperature was held constant. After correction, the sensors values agree within 1 mK and can be averaged together to obtain the sample's temperature. The uncertainty in the temperature read-out is obtained from the noise measurement (**Figure 6**, right red trace) and the uncertainty of absolute temperature is the sensor's interchangeability $uT = 0.1 + 0.0017|T + 273.15 \text{ K}|$.

At constant temperature, the nominal length L of the sample, which is given by the distance between the clamped sample mirrors, can be determined by taking advantage of the unequal arm length interferometer of our setup: a variation in frequency will cause a variation in both QPD phase signals and, therefore, an equivalent measured length, thus the nominal length can be expressed as

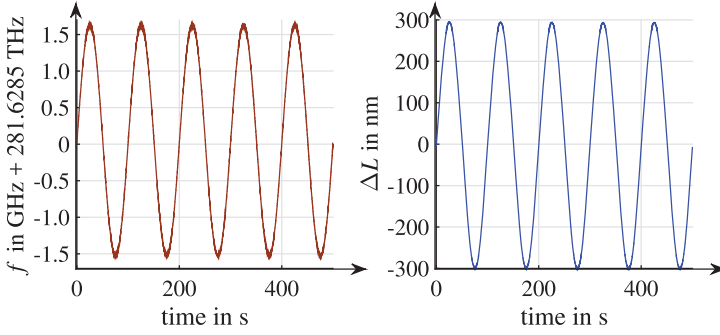


Figure 7. Measurements results for frequency variation (left) and induced length variation (right).

$$L = f \cdot \frac{\Delta L}{\Delta f}, \quad (9)$$

where the absolute frequency of the laser, f , its variations, Δf and ΔL were recorded simultaneously at a sampling frequency of 20 Hz. The frequency of the laser was measured by a wavelength-meter [HighFinesse WS6-600] while ΔL was measured by our phasemeter. The frequency of the laser was driven by a signal generator [Stanford Research SG384] to induce a sinusoidal frequency variation at 0.01 Hz with an amplitude of about 3 GHz (peak-to-peak) while the setup was held at $285.3 \text{ K} \pm 0.1 \text{ K}$.

Figure 7 shows the time-domain signals of the laser frequency and the interferometric length variations. Frequency variations of 1.5791 GHz resulted in ΔL changes of 293.45 nm. Using **Equation (9)** and the laser's mean frequency, $f = 281.6269 \text{ THz}$, the absolute length is calculated as

$$L = f \cdot \frac{\Delta L}{\Delta f} \pm \sqrt{\left| \frac{f \cdot u\Delta L}{\Delta f} \right|^2 + \left| \frac{f \cdot \Delta L \cdot u\Delta f}{(\Delta f)^2} \right|^2 + \left| \frac{\Delta L \cdot uf}{\Delta f} \right|^2}, \quad (10)$$

$$= 52.33 \text{ mm} \pm 0.02 \text{ mm}$$

where $u\Delta L = 40 \text{ pm}$ for $N = 10,000$ data points according to **Equation (6)** and **Figure 6** (right blue trace), the absolute frequency uncertainty is $uf = 400 \text{ MHz}$ and the frequency changes uncertainty is $u\Delta f = 400 \text{ kHz}$.

During this measurement, the wavefronts of the beams are not tilted physically, thus β_{QPD} does not play any role in the measurement and can be omitted.

4.2. Measurement at cycled temperature

In addition to the absolute length, one needs a temperature induced length change to calculate the CTE according to **Equation (1)**. For this, the sample's temperature is modulated by the thermal system in amplitude and cycle period, which ensures a homogeneous temperature distribution in the sample, similar to steady-state condition. As shown in **Figure 8**, the sample's temperature as well as its length variation have a period of 8 h, i.e., $34.72 \text{ } \mu\text{Hz}$ and has been applied for 5 cycles. The mean temperature of the three sensors is $T = 285.3 \text{ K} \pm 0.1 \text{ K}$ with an amplitude of $\Delta T = 2.04742 \text{ K} \pm 80 \mu\text{K}$ and a length variation of $\Delta L = 285 \text{ nm} \pm 1 \text{ nm}$. **Equation (1)** is used to calculate the CTE and its uncertainty due to errors in L , ΔL and ΔT , i.e.,

$$\alpha = \frac{1}{L} \cdot \frac{\Delta L}{\Delta T} \pm \sqrt{\left| \frac{\Delta L \cdot uL}{(L)^2 \cdot \Delta T} \right|^2 + \left| \frac{u\Delta L}{L \cdot \Delta T} \right|^2 + \left| \frac{\Delta L \cdot u\Delta T}{L \cdot (\Delta T)^2} \right|^2}, \quad (11)$$

$$= (2.66 \pm 0.01) \cdot 10^{-6} \text{ K}^{-1}$$

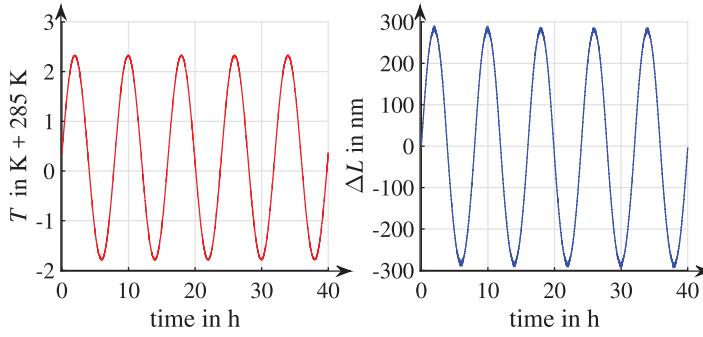


Figure 8. Measurement results for cycled temperature (left) and length variation (right).

which is significantly different from $\alpha = (2.485 \pm 0.004) \cdot 10^{-6} \text{ K}^{-1}$ ^[24] and other publications (e.g., $\alpha = (2.482 \pm 0.006) \cdot 10^{-6} \text{ K}^{-1}$,^[23] $\alpha = (2.48 \pm 0.01) \cdot 10^{-6} \text{ K}^{-1}$ ^[22]). The CTE estimation is biased with a difference of about 7%. Such bias was expected since, up to now, the TTL coupling has not been taken into account.

As discussed in Section 2, TTL coupling can have a significant effect on the ΔL measurement and thus in the CTE estimation. For this reason, the DWS signal must be taken into account. Figure 9 shows the tilt signals of both QPDs during the thermal cycling. The tilt signal of QPD1 follows a pattern synchronized to the applied 8-h cycle period; however, it does not follow a simple sinusoid. It is currently assumed to be from beam clipping caused by the sample and cannot be used. The tilt signal of QPD2 shows a clear 8-h cycle period in the temperature and length signals. Its amplitude is $19 \text{ nm} \pm 3 \text{ nm}$. By comparing the experimental results (Figure 8 and Figure 9) with the simulated ones shown in Section 2 (Figure 2) it is not clear what scenario took place during measurement since β_{QPD1} shows an abnormal response. Case (C) and case (D) are possible since β_{QPD2} signal shows the same sign as ΔT and ΔL . However, under scenario (C) the effect of the TTL should be three times larger and, consequently, the error in the CTE would be significantly larger than the 7% given by Equation (11). Thus, the result of Equation (11) indicates that the CTE is only slightly affected by TTL, which makes case (D) more likely, as we had previously assumed. Under such assumption, one can subtract η_{QPD2} from ΔL in order to correct for TTL, i.e.,

$$\alpha = \frac{\Delta L - \beta_{\text{QPD2}}}{L \cdot \Delta T} \pm \sqrt{\left| \frac{(\Delta L - \beta_{\text{QPD2}})uL}{(L)^2 \cdot \Delta T} \right|^2 + \left| \frac{u\Delta L}{L \cdot \Delta T} \right|^2 + \left| \frac{(\Delta L - \beta_{\text{QPD2}})u\Delta T}{L \cdot (\Delta T)^2} \right|^2 + \left| \frac{\beta_{\text{QPD2}} \cdot uk_{\text{QPD2}}}{k_{\text{QPD2}} \cdot L \cdot \Delta T} \right|^2 + \left| \frac{u\beta_{\text{QPD2}}}{L \cdot \Delta T} \right|^2},$$

$$= (2.48 \pm 0.03) \cdot 10^{-6} \text{ K}^{-1} \quad (12)$$

which is now in good agreement with the reference value $2.485 \cdot 10^{-6} \text{ K}^{-1}$ and shows that TTL introduces a systematic error that has to be taken into account to obtain accurate CTE values. Now, the bias is less than 1% with an $1-\sigma$ uncertainty and is mainly driven by $u\beta_{\text{QPD2}}$.

5. Conclusion and outlook

We have presented our improved dilatometer setup in order to mitigate errors in the CTE estimation due to TTL coupling. The method has been tested by measuring the CTE of a SCS sample at 285.3 K, which has a well-known CTE reported in the literature. The method to reduce TTL coupling relies on the interferometric signals measured by DWS from the QPDs, the calibration of the TTL coupling factor and, finally, the subtraction in post-processing of the TTL effect. The

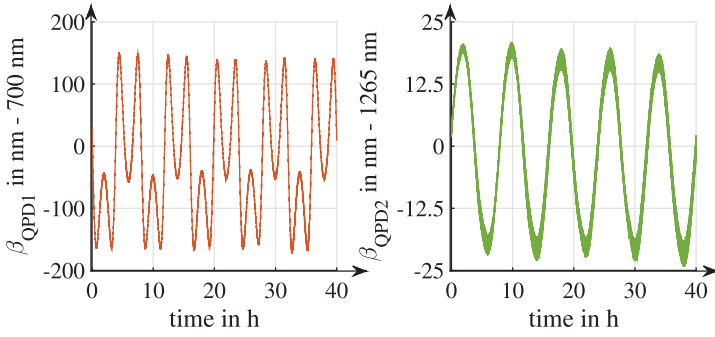


Figure 9. DWS measurement results at cycled temperature for QPD1 (left) and QPD2 (right). β_{QPD1} behavior deviates from what is expected and might be caused by beam clipping. In contrast, β_{QPD2} follows a sinusoidal shape with an 8 h cycling time.

CTE without TTL coupling subtraction exhibited a bias of about 7%, which was reduced to less than 1% after the TTL subtraction. This value, however, contains an intrinsic unknown uncertainty we currently cannot estimate the longitudinal motion of the tip-tilt mirror and beam position during calibration. Optical simulations have been also presented supporting our technique to correct the CTE.

The CTE result after TTL correction is $(2.48 \pm 0.03) \cdot 10^{-6} \text{ K}^{-1}$, which is in good agreement with the reference value^[24]: $(2.485 \pm 0.004) \cdot 10^{-6} \text{ K}^{-1}$. In our setup, the dominant source of uncertainty is due to the DWS read-out noise.

For future work, we plan to work on improvements for better tilt measurements. First, we need to adjust our setup to prevent beam clipping and achieve a pure sinusoidal signal from QPD. Second, we will reduce the tilt offset during measurement with a better setup alignment to avoid nonlinear effects of DWS. Third, we plan to investigate in more detail the impact of TTL and cross-coupling effects due to the beam position on the mirror to its rotational center during calibration compared to the sample measurement. All these three improvements increase the robustness of our measurement procedure.

Furthermore, we will characterize our sample at other temperatures to verify the correction scheme. Moreover, we intend to keep measuring other sample materials and compare measurement results with other metrological institutes.

Acknowledgments

For the TTL analyses in Section 3 and IfoCAD scientific development, we acknowledge support from the German Research Foundation DFG within SFB 1128 geo-Q (project A05).

References

- [1] Heinzel, G.; Braxmaier, C.; Schilling, R.; Rüdiger, A.; Robertson, D.; Plate, M.T.; Wand, V.; Arai, K.; Johann, U.; Danzmann, K. Interferometry for the LISA Technology Package (LTP) aboard SMART-2. *Class. Quantum Grav.* **2003**, *20*, S153.
- [2] Heinzel, G.; Wand, V.; García, A.; Jennrich, O.; Braxmaier, C.; Robertson, D.; Middleton, K.; Hoyland, D.; Rüdiger, A.; Schilling, R.; et al. The LTP interferometer and phasemeter. *Class. Quantum Grav.* **2004**, *21*, S581–S587.
- [3] Armano, M.; Audley, H.; Auger, G.; Baird, J.T.; Bassan, M.; Binetruy, P.; Born, M.; Bortoluzzi, D.; Brandt, N.; Caleno, M.; et al. Sub-Femto-g free fall for space-based gravitational wave observatories: LISA pathfinder results. *Phys. Rev. Lett.* **2016**, *116*, 231101.
- [4] Koch, A.; Sanjuan, J.; Gohlke, M.; Mahrtdt, C.; Brause, N.; Braxmaier, C.; Heinzel, G. Line of sight calibration for the laser ranging interferometer on-board the GRACE follow-on mission: On-ground experimental validation. *Opt. Express* **2018**, *26*, 25892–25908.

- [5] Sheard, S.B.; Heinzel, G.; Danzmann, K.; Shaddock, D.A.; Klipstein, W.; Folkner, W.M. Intersatellite laser ranging instrument for the GRACE follow-on mission. *J. Geod.* **2012**, *86*, 1083–1095.
- [6] Abich, K.; Bogan, C.; Braxmaier, C.; Danzmann, K.; Dehne, M.; Gohlke, M.; Göth, A.; Heinzel, G.; Herding, M.; Mahrtdt, C.; et al. GRACE-follow on laser ranging interferometer: German contribution. *J. Phys: Conf. Ser.* **2015**, *610*, 012010.
- [7] Fleddermann, R.; Ward, R.L.; Elliot, M.; Wuchenich, D.M.; Gilles, F.; Herding, M.; Nicklaus, K.; Brown, J.; Burke, J.; Dligatch, S.; et al. Testing the GRACE follow-on triple mirror assembly. *Class. Quantum Grav.* **2014**, *31*, 195004.
- [8] Gaia Collaboration. The GAIA mission. *Astron. Astrophys.* **2016**, *595*, A1.
- [9] Courteau, P.; Poupinet, A.; Kroedel, M.; Sarri, G. The HSOB GAIA: A cryogenic high stability cesic optical bench for missions requiring sub-nanometric optical stability. Proc. SPIE. **2006**, 10567, International Conference on Space Optics—ICSO 2006, 105670O.
- [10] Meijer, E.A.; Nijenhuis, J.N.; Vink, R.J.P.; Kamphues, F.; Gielesen, W.; Coatantiec, C. Pico meter metrology for the GAIA mission. Proc. SPIE **2009**, 7439, Astronomical and Space Optical Systems, 743915.
- [11] Sanjuán, J.; Korytov, D.; Mueller, G.; Spannagel, R.; Braxmaier, C.; Preston, A.; Livas, J. Note: Silicon carbide telescope dimensional stability and coefficient of thermal expansion investigations for space-based gravitational wave detectors. *Rev. Sci. Instrum.* **2012**, *83*, 116107.
- [12] Danzmann, K.; et.al. LISA laser interferometer space antenna – A proposal in response to the ESA call for L3 mission concepts. **2017**. https://www.elisascience.org/files/publications/LISA_L3_20170120.pdf
- [13] Spannagel, R.; Hamann, I.; Sanjuan, J.; Schuldt, T.; Gohlke, M.; Johann, U.; Weise, D.; Braxmaier, C. Dilatometer setup for low coefficient of thermal expansion materials measurements in the 140 K-250 K temperature range. *Rev. Sci. Instrum.* **2016**, *87*, 10.
- [14] Müller, H.; Chiow, S-W.; Long, Q.; Vo, C.; Chu, S. Active sub-rayleigh alignment of parallel or antiparallel laser beams. *Opt. Lett.* **2005**, *30*, 3323–3325.
- [15] Schuldt, T.; Braxmaier, C.; Müller, H.; Huber, G.; Peters, A.; Johann, U. Frequency stabilized Nd:YAG laser for space applications. Proceedings of the 5th International Conference on Space Optics (ICSO 2004), 30 March - 2 April 2004, Toulouse, Frankreich, **2004**.
- [16] Wanner, G.; Heinzel, G.; Kochkina, E.; Mahrtdt, C.; Sheard, B.S.; Schuster, S.; Danzmann, K. Methods for simulating the readout of lengths and angles in laser interferometers with Gaussian beams. *Opt. Commun.* **2012**, *285*, 4831–4839.
- [17] <http://www.lisa.aei-hannover.de/ifocad/>.
- [18] Wanner, G.; Schuster, S.; Tröbs, M.; Heinzel, G. A brief comparison of optical pathlength difference and various definitions for the interferometric phase. *J. Phys: Conf. Ser.* **2015**, *610*, 012043.
- [19] Heinzel, G.; Rüdiger, A.; Schilling, R. Spectrum and spectral density estimation by the Discrete Fourier transform (DFT), including a comprehensive list of window functions and some new at-top windows. **2002**. <http://hdl.handle.net/11858/00-001M-0000-0013-557A-5>
- [20] Hewitson, M.; Armano, M.; Benedetti, M.; Bogenstahl, J.; Bortoluzzi, D.; Bosetti, P.; Brandt, N.; Cavalleri, A.; Ciani, G.; Cristofolini, I.; et al. Data analysis for the LISA technology package. *Class. Quantum Grav.* **2009**, *26*, 094003.
- [21] Lyon, K.G.; Salinger, G.L.; Swenson, C.A.; White, G.K. Linear thermal expansion measurements on silicon from 6 to 340 K. *J. Appl. Phys.* **1977**, *48*, 865–868.
- [22] Swenson, C.A. Recommended values for the thermal expansivity of silicon from 0 to 1000 K. *J. Phys. Chem. Ref. Data* **1983**, *12*, 179–182.
- [23] Karlmann, P.B.; Klein, K.J.; Halverson, P.G.; Peters, R.D.; Levine, M.B.; Van Buren, D.; Dudik, M.J. Linear thermal expansion measurements of single crystal silicon for validation of interferometer based cryogenic dilatometer. *AIP Conf. Proc.* **2006**, *824*, 35–42.
- [24] Middelman, T.; Walkov, A.; Bartl, G.; Schödel, R. Thermal expansion coefficient of single-crystal silicon from 7 K to 293 K. *Phys. Rev. B* **2015**, *92*, 1–7.